LETTER

https://doi.org/10.1038/s41586-019-1028-3

# Attosecond angular streaking and tunnelling time in atomic hydrogen

U. Satya Sainadh[1], Han Xu[1]*, Xiaoshan Wang[2], A. Atia-Tul-Noor[1], William C. Wallace[1], Nicolas Douguet[3,6], Alexander Bray[4], Igor Ivanov[5], Klaus Bartschat[3], Anatoli Kheifets[4], R. T. Sang[1]* & I. V. Litvinyuk[1]*

**The tunnelling of a particle through a potential barrier is a key feature of quantum mechanics that goes to the core of wave–particle duality. The phenomenon has no counterpart in classical physics, and there are no well constructed dynamical observables that could be used to determine 'tunnelling times'. The resulting debate[1–5] about whether a tunnelling quantum particle spends a finite and measurable time under a potential barrier was reignited in recent years by the advent of ultrafast lasers and attosecond metrology[6]. Particularly important is the attosecond angular streaking ('attoclock') technique[7], which can time the release of electrons in strong-field ionization with a precision of a few attoseconds. Initial measurements[7–10] confirmed the prevailing view that tunnelling is instantaneous, but later studies[11,12] involving multi-electron atoms—which cannot be accurately modelled, complicating interpretation of the ionization dynamics—claimed evidence for finite tunnelling times. By contrast, the simplicity of the hydrogen atom enables precise experimental measurements and calculations[13–15] and makes it a convenient benchmark. Here we report attoclock and momentum-space imaging[16] experiments on atomic hydrogen and compare these results with accurate simulations based on the three-dimensional time-dependent Schrödinger equation and our experimental laser pulse parameters. We find excellent agreement between measured and simulated data, confirming the conclusions of an earlier theoretical study[17] of the attoclock technique in atomic hydrogen that presented a compelling argument for instantaneous tunnelling. In addition, we identify the Coulomb potential as the sole cause of the measured angle between the directions of electron emission and peak electric field: this angle had been attributed[11,12] to finite tunnelling times. We put an upper limit of 1.8 attoseconds on any tunnelling delay, in agreement with recent theoretical findings[18] and ruling out the interpretation of all commonly used 'tunnelling times'[19] as 'time spent by an electron under the potential barrier'[20].**

The attoclock technique utilizes a nearly circularly polarized few-cycle infrared pulse such that the vector of the evolving electric field, $\boldsymbol{E}(t)$, rotating by 360°, maps time to angle in the polarization plane (see Fig. 1). The technique was envisaged on the basis of a simple model of photoionization in strong laser fields[21,22], with the electron first tunnelling through the suppressed Coulomb potential in the presence of a strong external field, $\boldsymbol{E}(t)$. Then, from the instant the electron appears in the continuum, it moves classically in the electromagnetic field of the laser (streaking) and the Coulomb potential of the parent ion. As the ionizing radiation that releases the electron and the streaking field are provided by the same laser pulse, the technique is self-referencing. The pronounced nonlinearity of tunnelling ionization ensures that the ionization rate peaks when $\boldsymbol{E}(t)$ reaches its maximum, with the streaking field driving the emitted electron so that its final momentum (following the interaction with the pulse) is equal to the negative instantaneous value of the vector potential, $\boldsymbol{A}(t)$, of the streaking field at the moment of ionization. The instant of maximum field thus serves as well-defined 'time zero' of the attoclock, while the instant of ionization—which might be regarded as 'tunnel exit'—is encoded onto the free electron's momentum. We find that the time interval between those two instances, often interpreted as tunnelling delay, is zero for atomic hydrogen.

Although angular streaking works best with circularly polarized few-cycle pulses, the angle at which the electric field (and hence the tunnelling ionization probability) reaches its maximum depends on the carrier-envelope phase (CEP) that with state-of-the-art stabilization techniques has a noise of about 100–150 mrad. This noise corresponds to an uncertainty of about 7° or 50 attoseconds (as) in measured angle or time, respectively, a value comparable to or even exceeding the expected time delays. This difficulty is avoided when using slightly elliptically polarized light pulses where, even for an ellipticity of 0.88 (very close to circular) and without CEP stabilization, the electric field will reach its maximum when pointing along the major axis of the polarization ellipse[8]. Because the direction of the electric field can be established with high precision using basic polarimetry, the instance of maximum field can be accurately determined.

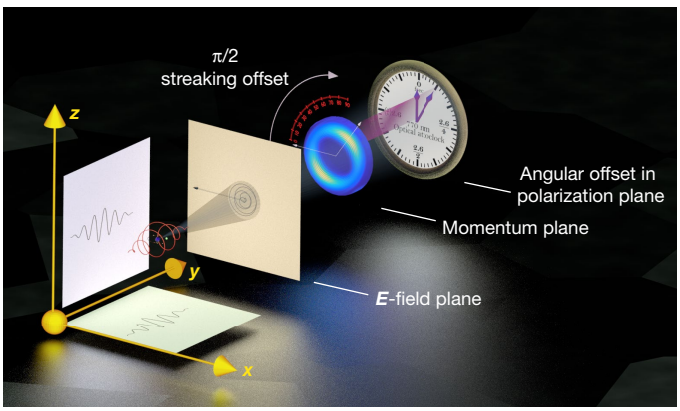


**Fig. 1 | Attosecond angular streaking.** A few-cycle nearly circularly polarized pulse provides a unique direction for the maximal field vector in the polarization plane, where the ionization probability is maximum. The vector-potential trails the rotating $\boldsymbol{E}$-vector (represented by the red spiral around a hydrogen atom at left and its projection onto the $\boldsymbol{E}$-field plane) by 90° and hence the electron is emitted perpendicularly to the instantaneous direction of the $\boldsymbol{E}$-field at the moment of ionization, as illustrated by the π/2 streaking offset. However, any delay between the electron's exit and an independently measured peak $\boldsymbol{E}$-field, either due to scattering by Coulomb potential or the tunnelling time, manifests as measurable angular offset in the photoelectron momentum distribution (PMD, shown in the momentum plane). Since an optical cycle for 770 nm is 2.6 fs, 1° in offset angle corresponds to 7.13 as in the electron ionization delay, directly mapping time to angle as read from the attoclock dial at right.

[1]Australian Attosecond Science facility, Centre for Quantum Dynamics, Griffith University, Nathan, Queensland, Australia. [2]School of Nuclear Science and Technology, Lanzhou University, Lanzhou, China. [3]Department of Physics and Astronomy, Drake University, Des Moines, IA, USA. [4]Research School of Physics and Engineering, The Australian National University, Canberra, Australian Capital Territory, Australia. [5]Centre for Relativistic Laser Science, Institute for Basic Science, Gwangju, South Korea. [6]Present address: Department of Physics, University of Central Florida, Orlando, FL, USA. *e-mail: h.xu@griffith.edu.au; r.sang@griffith.edu.au; i.litvinyuk@griffith.edu.au

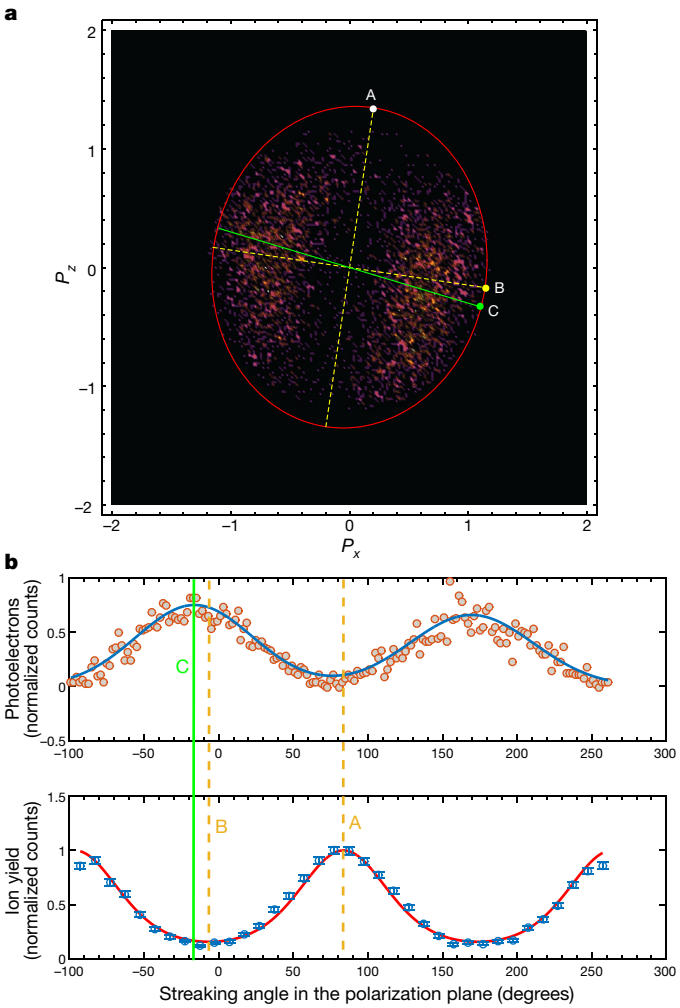


**Fig. 2 | Angular offsets.** The presented data are for a peak intensity of $1.95 \times 10^{14}$ W cm$^{-2}$. **a**, PMD in the polarization plane, where A corresponds to the peak ***E***-field, and B and C are, respectively, the expected and measured position of peak PMD. $P_x$ and $P_z$ are two components of electron momentum in the laser polarization plane. **b**, Top, radially integrated photoelectron signal in angular bins of 2°, fitted with a double Gaussian function (blue line) determining the peak position of PMD (green vertical line). Bottom, atomic H-ion yield data as a function of calibrated polarizer angle (blue circles represent measurements, red line is the fit), used to determine the major axis of the polarization ellipse (yellow dashed vertical line marked A; a similar line marked B represents the minor axis of the ellipse, see Methods and Extended Data Fig. 2). The points A, B and C are shown in **a** and **b**, illustrating a measured angular offset of 10.87° ± 1.42° between B and C.

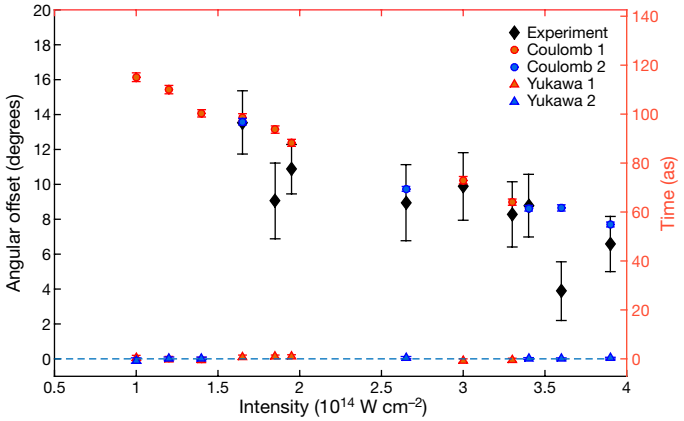


**Fig. 3 | Results of our experiments and simulations.** The experimental observations (black diamonds with estimated experimental and fitting errors) are compared to ab initio 3D-TDSE simulations with Coulomb potentials provided by two independent groups marked as 1 and 2 (respectively orange and blue filled circles). To disentangle the effects of the Coulomb potential on the continuum electron, we also include the TDSE simulations for a Yukawa potential (orange and blue filled triangles representing calculations by the same two independent groups marked as 1 and 2). Numerical errors are comparable to or less than the symbol size. The horizontal dashed blue line is drawn at the zero offset angle. The same extraction procedure was used to determine the offset angles from experimental results and theoretical simulations for both Coulomb and Yukawa potentials. Our numerical experiment demonstrates that the observed angular offsets are entirely due to the electron scattering by the long-range Coulomb potential of the ion.

Our experiment uses laser pulses that are centred at 770 nm with 6 fs duration and ellipticity of 0.84 ± 0.01, and an atomic H jet that is generated in a discharge source achieving 50% dissociation and integrated with a reaction microscope (REMI, see Methods and Extended Data Fig. 1 for full details). Once the polarization ellipse is defined, we ionize H from the atomic gas jet and detect each electron–proton pair in coincidence. To ensure that electron–proton pairs originate from the same H atom, conditions are adjusted to keep the ionization events per pulse low enough that the false coincidence probability is less than 4%. Data were then collected with laser pulses whose peak intensity was varied from $1.65 \times 10^{14}$ W cm$^{-2}$ to $3.9 \times 10^{14}$ W cm$^{-2}$, with Fig. 2 illustrating how angular offsets were extracted from our experimental data for an intensity of $1.95 \times 10^{14}$ W cm$^{-2}$.

The attoclock observables from the experiment are directly compared to ab initio simulations by two independent theoretical groups. The full solutions of the three-dimensional time-dependent Schrödinger equation (3D-TDSE), calculated accurately within the non-relativistic framework using the electric dipole approximation and using experimental pulse parameters, generate photoelectron momentum distributions (PMD) projected on the polarization plane. Since the CEP was not stabilized in our experiments, the simulations average the momentum distributions over eight CEP values ranging from 0 to 2π in steps of π/4. The calculated momentum spectra are then analysed exactly as their experimental counterparts, with Fig. 3 comparing the theoretically and experimentally determined angular offsets. The error bars associated with the theoretical data are due to uncertainties in our fitting procedure used to determine the angular offsets.

The experimental and simulation results (the latter from two independent calculations) are in an excellent agreement, all showing a decrease in angular offset as the field strength increases. The Coulomb potential itself is known to give rise to angular offsets in the momentum distributions of electrons ionized by an elliptically polarized field, and it is therefore critical to disentangle the effect of the Coulomb potential on the measured delay. Although the Coulomb potential cannot be removed or replaced by a different potential in an experiment, this can be easily done in theoretical simulations using a short-range Yukawa potential that is modelled as $U_Y = -(Z/r) \times e^{-r/a}$ and with parameters $Z = 1.908$ and $a = 1$ to preserve the ground-state energy of the system (see Extended Data Fig. 3). The PMDs simulated with this potential and using the experimental pulse parameters give a zero angular offset (within our numerical and fitting uncertainty) for all intensities, showing that for atomic H the non-zero offset angles originate entirely from Coulomb scattering of the ejected electron and that there is zero time delay between the appearance of the peak of the electric field and the appearance of the peak density of the continuum electron wave packet measured by the attoclock.

Our estimated experimental and numerical uncertainties allow us to put an upper bound on the time delays: considering data derived with the Yukawa potential, we find the angular offset that has deviated most from the zero reference line. We estimate that the angular offset cannot exceed 0.25° for the Yukawa potential, which corresponds to a maximum possible time delay of 1.8 as. This value is substantially less

than the tens to few hundreds of attoseconds expected for commonly used theoretical definitions of tunnelling time[19] (that is, Keldysh time, Büttiker–Landauer time, Eisenbud–Wigner time, Pollack–Miller time, Larmor time, Bohmian time), which are thus effectively ruled out as being interpretable as the 'time spent by a quantum particle under a potential barrier'.

Our findings do not invalidate the finite delay times inferred from earlier experiments on multi-electron systems[11,12], but rule out explanations invoking one-electron tunnelling dynamics and thus call for alternative explanations (with multi-electron dynamics being the most likely cause[17]). In closing, we note that as tunnelling events in strong-field ionization of H are only as 'instantaneous' as the electron wavefunction collapse that orthodox interpretations of quantum mechanics associate with the appearance of continuum electrons, future measurements of tunnelling in the zeptosecond ($10^{-21}$ s) or sub-zeptosecond domain raise the intriguing possibility of obtaining information on the dynamics of the wavefunction collapse itself.

## Online content

Any methods, additional references, Nature Research reporting summaries, source data, statements of data availability and associated accession codes are available at https://doi.org/10.1038/s41586-019-1028-3.

Received: 26 July 2017; Accepted: 7 January 2019;
Published online: 18 March 2019

1. Wigner, E. P. Lower limit for the energy derivative of the scattering phase shift. *Phys. Rev.* **98**, 145–147 (1955).
2. Smith, F. T. Lifetime matrix in collision theory. *Phys. Rev.* **118**, 349–356 (1960).
3. Büttiker, M. & Landauer, R. Traversal time for tunneling. *Phys. Rev. Lett.* **49**, 1739–1742 (1982).
4. Mandelstam, L. & Tamm, I. The uncertainty relation between energy and time in nonrelativistic quantum mechanics. *J. Phys.* **9**, 249–254 (1945).
5. Yamada, N. Speakable and unspeakable in the tunneling time problem. *Phys. Rev. Lett.* **83**, 3350–3353 (1999).
6. Hentschel, M. et al. Attosecond metrology. *Nature* **414**, 509–513 (2001).
7. Eckle, P. et al. Attosecond angular streaking. *Nat. Phys.* **4**, 565–570 (2008).
8. Eckle, P. et al. Attosecond ionization and tunneling delay time measurements in helium. *Science* **322**, 1525–1529 (2008).
9. Pfeiffer, A. N. et al. Attoclock reveals natural coordinates of the laser-induced tunnelling current flow in atoms. *Nat. Phys.* **8**, 76–80 (2012).
10. Pfeiffer, A. N., Cirelli, C., Smolarski, M. & Keller, U. Recent attoclock measurements of strong field ionization. *Chem. Phys.* **414**, 84–91 (2013).
11. Camus, N. et al. Experimental evidence for quantum tunneling time. *Phys. Rev. Lett.* **119**, 023201 (2017).
12. Landsman, A. S. et al. Ultrafast resolution of tunneling delay time. *Optica* **1**, 343–349 (2014).
13. Kielpinski, D., Sang, R. & Litvinyuk, I. Benchmarking strong-field ionization with atomic hydrogen. *J. Phys. At. Mol. Opt. Phys.* **47**, 204003 (2014).
14. Wallace, W. et al. Precise and accurate measurements of strong-field photoionization and a transferable laser intensity calibration standard. *Phys. Rev. Lett.* **117**, 053001 (2016).
15. Khurmi, C. et al. Measuring laser carrier-envelope phase effects in the noble gases with an atomic hydrogen calibration standard. *Phys. Rev. A* **96**, 013404 (2017).
16. Dörner, R. et al. Cold target recoil ion momentum spectroscopy: a 'momentum microscope' to view atomic collision dynamics. *Phys. Rep.* **330**, 95–192 (2000).
17. Torlina, L. et al. Interpreting attoclock measurements of tunnelling times. *Nat. Phys.* **11**, 503–508 (2015).
18. Ni, H., Saalmann, U. & Rost, J.-M. Tunneling ionization time resolved by backpropagation. *Phys. Rev. Lett.* **117**, 023002 (2016).
19. Zimmermann, T., Mishra, S., Doran, B. R., Gordon, D. F. & Landsman, A. S. Tunneling time and weak measurement in strong field ionization. *Phys. Rev. Lett.* **116**, 233603 (2016).
20. Ni, H., Saalmann, U. & Rost, J.-M. Tunneling exit characteristics from classical backpropagation of an ionized electron wave packet. *Phys. Rev. A* **97**, 013426 (2018).
21. Corkum, P. B. Plasma perspective on strong field multiphoton ionization. *Phys. Rev. Lett.* **71**, 1994–1997 (1993).
22. Kulander, K., Schafer, K. & Krause, J. in *Super-Intense Laser–Atom Physics* 95–110 (Plenum Press, New York, 1993).

**Acknowledgements** The experiments were performed at the Australian Attosecond Science Facility at Griffith University. We acknowledge the traditional custodians of the land on which this work was undertaken at Griffith University, the Yuggera people, and at ANU, the Ngunnawal people. U.S.S. and A.A.-T.-N. were supported by Griffith University International Postgraduate Research Scholarships (GUIPRS). H.X. was supported by an Australian Research Council Discovery Early Career Researcher Award (ARC DECRA: DE130101628). The work of N.D. and K.B. was supported by the United States National Science Foundation under grant no. PHY-1430245 and XSEDE allocation PHY-090031: their calculations were performed on SuperMIC at the Center for Computation and Technology at Louisiana State University. I.I. was supported by the Institute for Basic Science under grant number IBS-R012-D1.

**Author contributions** U.S.S., X.W. and W.C.W. integrated the hydrogen source with REMI as part of the experimental set-up. U.S.S. with the assistance of H.X. and A.A.-T.-N. performed the experiments. U.S.S. and H.X. analysed the experimental data and post-processed theoretical data. Theoretical predictions were provided by A.B., A.K., I.I., N.D. and K.B. The project was conceived and supervised by R.T.S. and I.V.L. All authors discussed the results and contributed to the manuscript, with I.V.L. overseeing its preparation and revisions.

**Competing interests** The authors declare no competing interests.

**Additional information**
**Extended data** is available for this paper at https://doi.org/10.1038/s41586-019-1028-3.
**Reprints and permissions information** is available at http://www.nature.com/reprints.
**Correspondence and requests for materials** should be addressed to H.X., R.T.S. or I.V.L.
**Publisher's note:** Springer Nature remains neutral with regard to jurisdictional claims in published maps and institutional affiliations.

## METHODS

**Experimental details and set-up.** We create an atomic H jet using a radio-frequency (RF) discharge tube based on the design[23] that dissociates hydrogen molecules via electron impact. Hydrogen gas from the cylinder is sent through a Pyrex glass tube mounted inside a quarter-wave helical resonator, which is powered with an amplified RF signal at 75 MHz. The standing wave formed in the tube strikes a discharge, generating a plasma which dissociates molecular hydrogen. The discharge produces a beam of atomic hydrogen with a constant dissociation fraction $\mu$, defined by the number density of atomic and molecular hydrogen as:

$$\mu = \frac{[\mathrm{H}]}{[\mathrm{H}] + 2[\mathrm{H_2}]} \tag{1}$$

In the experiment, we generated H with a dissociation fraction of 50%. Further details on the construction, operation, characterization and optimization of this apparatus are available elsewhere[24]. Before it reaches the interaction region, the hydrogen beam passes between two deflector plates used to remove any charged particles from the beam by applying a constant electric field of 26 V cm$^{-1}$ over 6 cm length. That electric field also serves to quench any metastable hydrogen atoms (mostly 2*s* H) produced during dissociation (see Methods section 'Excited states of H' for details).

We generate 6 fs pulses (full-width at half-maximum) with 770 nm central wavelength using the 'Femtopower Compact Pro CE-Phase' laser system (FEMTOLASERS Produktions GmbH) with a Ne-filled hollow-core fibre compressor that has a repetition rate of 1 kHz. Ions and electrons formed by the ionization of hydrogen atoms interacting with these laser pulses are detected in coincidence in the reaction microscope (REMI) apparatus. We ensure that less than one ionization event occurs for every laser pulse and analyse only the electrons coincident with very low-energy protons characteristic of atomic H ionization.

**Analysis of data and results.** The projected PMD in the polarization plane ($P_x$–$P_z$) is divided into optimal polar angular bins $\Delta\theta$, where $\theta$, defined as $\tan^{-1}(P_z/P_x)$, is the streaking angle. The distribution acquired by radially integrating the counts in each bin, $f(\theta)$, is plotted against the streaking angle and is then fitted using a double Gaussian function of the form

$$f(\theta) = \sum_{i=1}^{2} a_i \mathrm{e}^{-\left[\frac{\theta - b_i}{c_i}\right]^2} \tag{2}$$

using a least-squares fitting routine. The values of $b_i$ give the direction of most probable ejection ($\theta_{\mathrm{streak}}$); and the fitting procedure provides 95% ($2\sigma$) level confidence bounds of the fit from which the standard error, $\delta\theta_{\mathrm{streak}}$ is inferred.

The angular offset is defined as the angular difference between the direction of the maximum of the photoelectron angular distribution and that of the maximum field. However, the maximum field is determined using polarimetry in the polarizer's reference frame and the PMD is measured in REMI's frame of reference. In order to have an absolute comparison of the measured angles in the polarization measurement and the angular distributions, we use a polarizer to convert the laser pulse into linear polarization before sending it into REMI to ionize atomic H. Since with linearly polarized field, the electrons are mainly emitted along the laser polarization axis, which is parallel to the polarizer's optical axis, we calibrate the angle of the polarizer's optical axis with the angle of the peak PMD measured in the REMI's coordinate system (see Extended Data Fig. 2). The angle of peak PMD is extracted using the above described double Gaussian fit routine, and a relative offset of $\theta_{\mathrm{sys}}$ with an error of $\delta\theta_{\mathrm{sys}}$ between the two coordinate systems is determined. This enabled us to work in the same frame of reference such that the relation is $\theta = \theta_{\mathrm{pol}} - \theta_{\mathrm{sys}}$, where $\theta_{\mathrm{pol}}$ is the angle of the polarizer's optical axis.

We then performed optical polarimetry measurements, with the calibrated angle, to determine the ellipticity by using H ion yields in the polarization plane to find the major axis of the polarization ellipse. Given the highly nonlinear dependence of the ionization probability as a function of the electric field, this mechanism provides a more accurate determination of the polarization ellipse for day-to-day measurements. We extracted the ellipticity of the polarization ellipse through fitting with the function:

$$P(\theta) = A^2 \sin^2(\theta - c) + B^2 \cos^2(\theta - c) \tag{3}$$

Here $B/A$ gives the ellipticity, manifested as the modulation depth, while $c$ gives the angle at which the polarization ellipse, that is, the major axis, was oriented. The ellipticity is defined as $\varepsilon =$ major axis/minor axis (of the $\boldsymbol{E}$-field, which is proportional to the square root of the intensity), such that it spans the range from 0 to 1 corresponding to linear and circular polarization, respectively. The error in ellipticity is calculated as $\delta\varepsilon/\varepsilon = \sqrt{(\delta B/B)^2 + (\delta A/A)^2}$, where $\delta B$ ($\delta A$) are the standard errors extracted from the fits. To find the major axis we used the fitting function $\mathrm{e}^{-P(\theta)}$ that fits the atomic H ion yields.

The error in the determining the relative offset in the calibration procedure contributes to the error in the fit, $\delta\theta_{\mathrm{fit}}$, to give us $\delta\theta_{\mathrm{ellipse}} = \sqrt{\delta\theta_{\mathrm{sys}}^2 + \delta\theta_{\mathrm{fit}}^2}$. Having both the measurements precisely taken in the same frame of reference enables the angular offset and its corresponding error to be determined via

$$\theta_{\mathrm{offset}} = \theta_{\mathrm{streak}} - \theta_{\mathrm{ellipse}} - 90^\circ \tag{4}$$

$$\delta\theta_{\mathrm{offset}} = \sqrt{\delta\theta_{\mathrm{ellipse}}^2 + \delta\theta_{\mathrm{streak}}^2} \tag{5}$$

where $\theta_{\mathrm{streak}}$ and $\theta_{\mathrm{ellipse}}$ are defined as the direction of the most probable photoelectron ejection and orientation of the major axis in the polarization plane, respectively. Here the streaking angle of the light pulse is −90°, since the momentum of the streaked electrons is determined by the vector potential of the light field of the pulse, which itself lags the electric field by 90°.

**Numerical simulations.** The numerical methods employed by two groups to solve the 3D-TDSE are conceptually similar, both relying on spherical-harmonics expansions of the wavefunction to represent its dependence on the angular variables and treating the radial variable by discretizing the TDSE on a grid. Both groups used the matrix iterative method[25] to propagate the initial state in time using the velocity gauge in the electric dipole approximation. Detailed descriptions of the numerical techniques used by the two groups can be found elsewhere[26,27]. Careful checks were performed to ensure that convergence with respect to the parameters defining the accuracy of the calculation (for example, the number of partial waves in the expansion as well as the step sizes on the space-time grid) was achieved. For the peak intensity of $1.65 \times 10^{14}$ W cm$^{-2}$, the results from the two groups were compared to ensure that the independent implementations of the computational techniques gave the same result within the error bar due to the uncertainty of the fitting procedure used to determine the angular offset. The maximum orbital angular momentum $l_{\mathrm{max}}$ needed in the partial-wave expansion was 40 for $1.4 \times 10^{14}$ W cm$^{-2}$ and 100 for $3.9 \times 10^{14}$ W cm$^{-2}$, respectively. Specifically, we set the components of the vector potential $\boldsymbol{A}(t)$ for a pulse with ellipticity $\varepsilon$ as:

$$A_x(t) = -\frac{E_0}{\omega} f(t) \frac{\varepsilon}{\sqrt{1+\varepsilon^2}} \cos(\omega t + \varphi) \tag{6}$$

$$A_y(t) = -\frac{E_0}{\omega} f(t) \frac{1}{\sqrt{1+\varepsilon^2}} \sin(\omega t + \varphi) \tag{7}$$

$$A_z(t) = 0 \tag{8}$$

The envelope function $f(t)$ was a Gaussian ramped on and off over three optical cycles each, respectively. The electric field was obtained as $\boldsymbol{E}(t) = -\mathrm{d}\boldsymbol{A}(t)/\mathrm{d}t$. Finally, the carrier envelope phase $\varphi$ was varied in steps of $\pi/4$ and the results were averaged.

**Excited states of H.** Discharge dissociation of $H_2$ by electron impact can produce electronically excited hydrogen atoms via dissociation of excited hydrogen molecules. Most of those excited states will decay radiatively into 1*s* or 2*s* states within few nanoseconds. The 2*s* state is metastable (its radiative one-photon transition to the ground state is forbidden by the selection rules) with field-free lifetime of one-seventh of a second[28] determined by the rate of the two-photon transition. However, that restriction is lifted by an external electric field which couples 2*s* and 2*p* states, thus effectively quenching the 2*s*.

The lifetime of H 2*s* as a function of external electric field $E$ was calculated by Bethe and Salpeter (section 67 of ref. [28]) and the theoretical formula was experimentally verified by Sellin[29]. That lifetime is given by

$$\tau(E) = \tau(2p)\left\{1 + \frac{\delta^2}{[1-(1+\delta^2)^{1/2}]^2}\right\}, \quad \delta = \frac{2\sqrt{3Eea_0}}{L} \tag{9}$$

where $\tau(2p)$ is the lifetime of the 2*p* state, $L$ is the Lamb shift, $a_0$ is the Bohr radius and $e$ is the electron charge.

For the electric field of 23 V cm$^{-1}$ present inside our spectrometer, the lifetime of H 2*s* is less than 700 ns. It is even less for the field of 26 V cm$^{-1}$ that exists between the 6 cm deflector plates used to remove charged particles from our beam. For a typical beam velocity of 2,500 m s$^{-1}$, hydrogen atoms will travel less than 2 mm during the lifetime of H 2*s*, with the population of H 2*s* reduced by a factor of e along the way. As the atoms need to cover 10 cm through the electric field (6 cm between the deflector plates and 4 cm inside the spectrometer) to reach the laser focus, the population of H 2*s* will be reduced by the factor of at least e$^{50}$ or $10^{22}$ to essentially zero.

It is easy to confirm the absence of H 2*s* in the interaction region, due to their electron momentum distributions being very distinct from those of H 1*s*.

We calculated those momentum distributions for the same pulse parameters using the same numerical simulation methods (see Extended Data Fig. 4). Owing to its much lower ionization potential H 2*s* is ionized early in the pulse, so that the electrons gain less energy from the field. In addition to lower energy, the angular distribution of the H 2*s* electron is nearly uniform. Even if a significant fraction of the signal came from H 2*s*, the measured offset angles would not have been affected—only the modulation depth of the angular distribution would be diminished. However, the modulation depth measured in our experiments agrees with the theoretical prediction for pure H 1*s*, indicating that there is very little, if any, H 2*s* in our target gas. Furthermore, we calculated the offset angles with the energy filter removing H 2*s* electrons imposed and obtained the same values within the error bars as before.

## Data availability

The data that support the findings of this study are available from the corresponding authors on reasonable request.


23. Slevin, J. & Stirling, W. Radio frequency atomic hydrogen beam source. *Rev. Sci. Instrum.* **52**, 1780–1782 (1981).
24. Pullen, M. G. *Above Threshold Ionisation of Atomic Hydrogen Using Few-Cycle Pulses*. Thesis, Griffith Univ. (2011).
25. Nurhuda, M. & Faisal, F. H. Numerical solution of time-dependent Schrödinger equation for multiphoton processes: a matrix iterative method. *Phys. Rev. A* **60**, 3125–3133 (1999).
26. Douguet, N. et al. Photoelectron angular distributions in bichromatic atomic ionization induced by circularly polarized VUV femtosecond pulses. *Phys. Rev. A* **93**, 033402 (2016).
27. Ivanov, I. Evolution of the transverse photoelectron-momentum distribution for atomic ionization driven by a laser pulse with varying ellipticity. *Phys. Rev. A* **90**, 013418 (2014).
28. Bethe, H. A. & Salpeter, E. E. *Quantum Mechanics of One-and Two-Electron Atoms* (Springer, Berlin, 1957).
29. Sellin, I. Experiments on the production and extinction of the 2s state of the hydrogen atom. *Phys. Rev*. **136**, A1245–A1253 (1964).

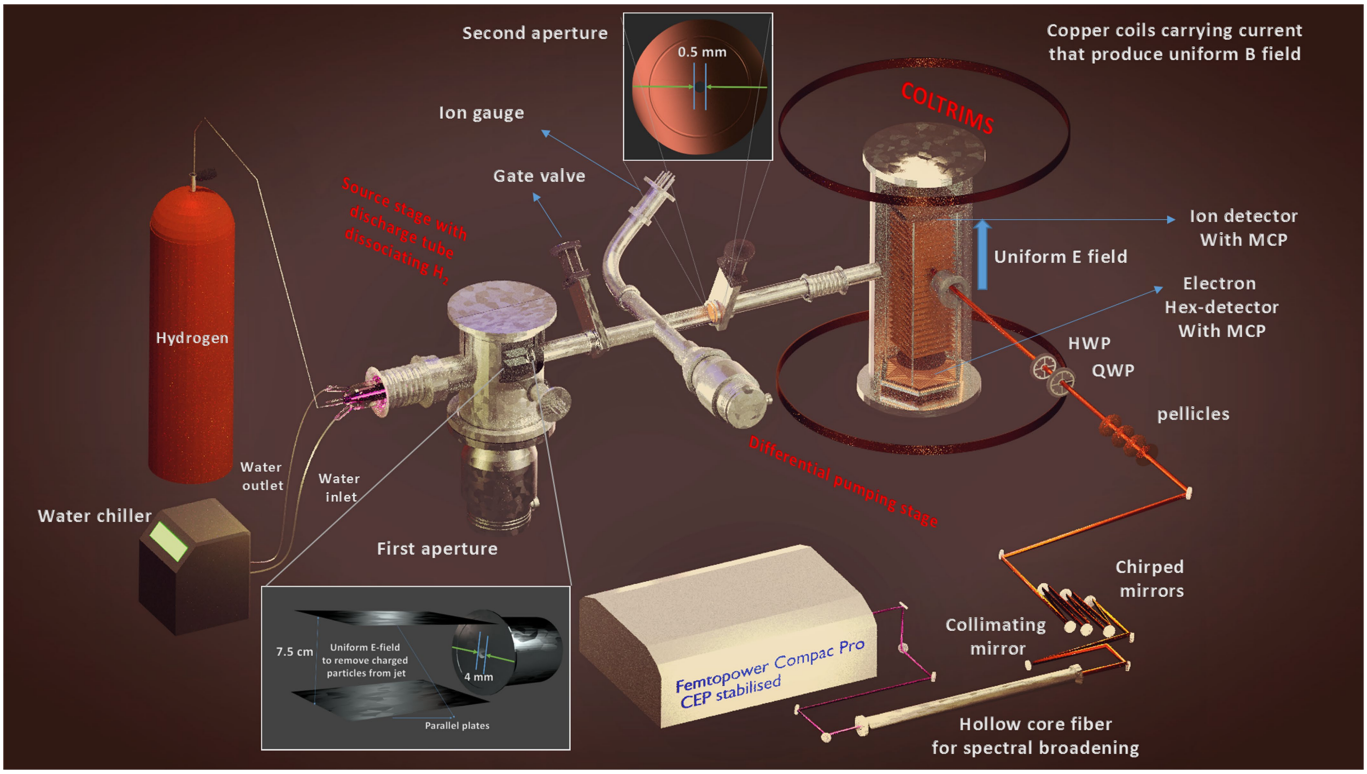


**Extended Data Fig. 1 | Experimental set-up.** As part of the atomic beamline, the water-cooled Pyrex discharge tube (connected by a gas line directly to the hydrogen cylinder) dissociates $H_2$ to H. Any charged species leaving the tube are expelled by a uniform electric field before the beam enters the differential pumping stage through the first aperture (see inset). The beam then enters the REMI through a 0.5 mm aperture (second aperture; see inset) as a supersonic jet. The laser pulses pass through a series of pellicle beamsplitters (that vary intensity) and ultra-broadband waveplates (that introduce ellipticity) before interacting with H in the REMI. Ionized fragments are accelerated in uniform electric-magnetic fields and are finally detected on position sensitive detectors, helping to reconstruct the 3D-momentum distribution of the fragments. HWP, half-wave plate; QWP, quarter-wave plate; MCP, microchannel plates; hex-detector, hexagonal delay-line-anode detector.

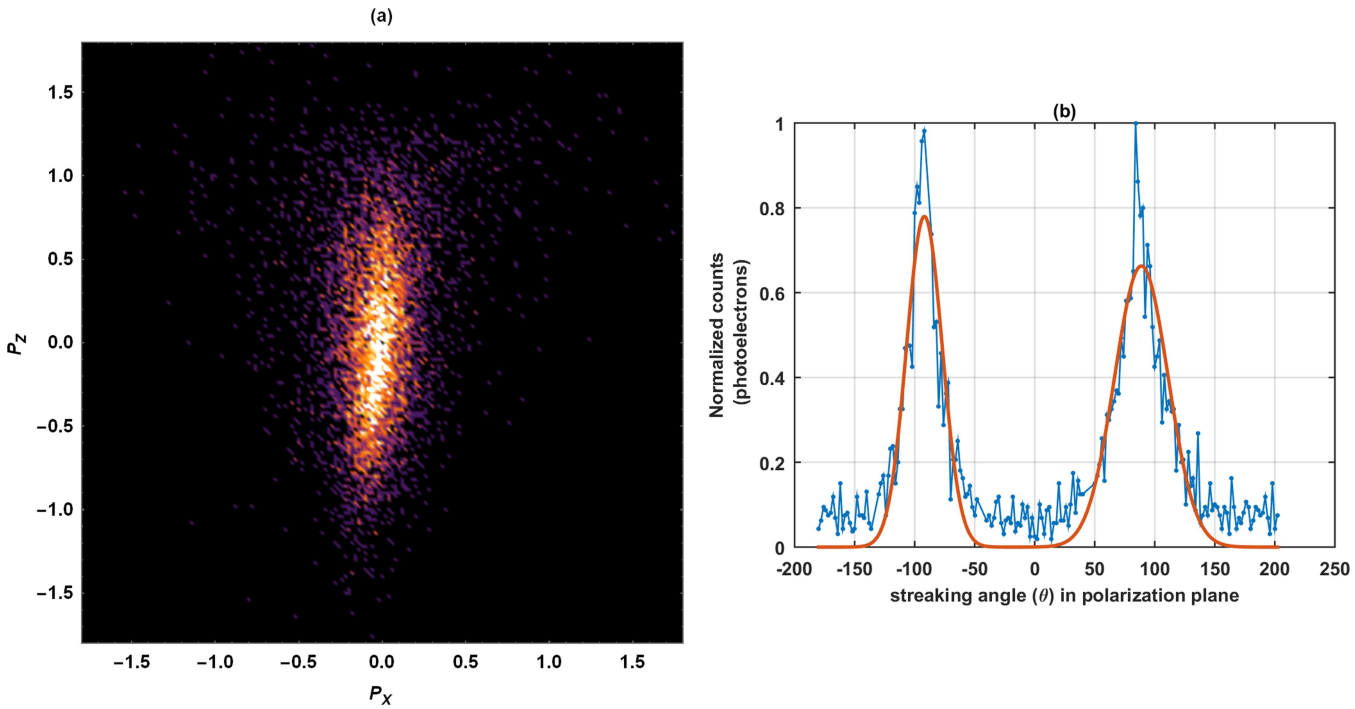


**Extended Data Fig. 2 | Calibration of the reference frame.** The elliptically polarized few-cycle pulse is passed through a polarizer aligned vertically, and then made to interact with the atomic jet inside the REMI (**a**). The orientation of the field is found by determining the peaks of the PMD as a function of streaking angle (**b**), thereby giving us a systematic offset between the polarizer's frame and REMI's frame. The polarization is chosen parallel to the time-of-flight axis because of better momentum resolution in this direction. A systematic offset of about 3° was measured and used to calibrate our measured offsets and polarimetry. See Methods section 'Analysis of data and results' for details of this calibration procedure.

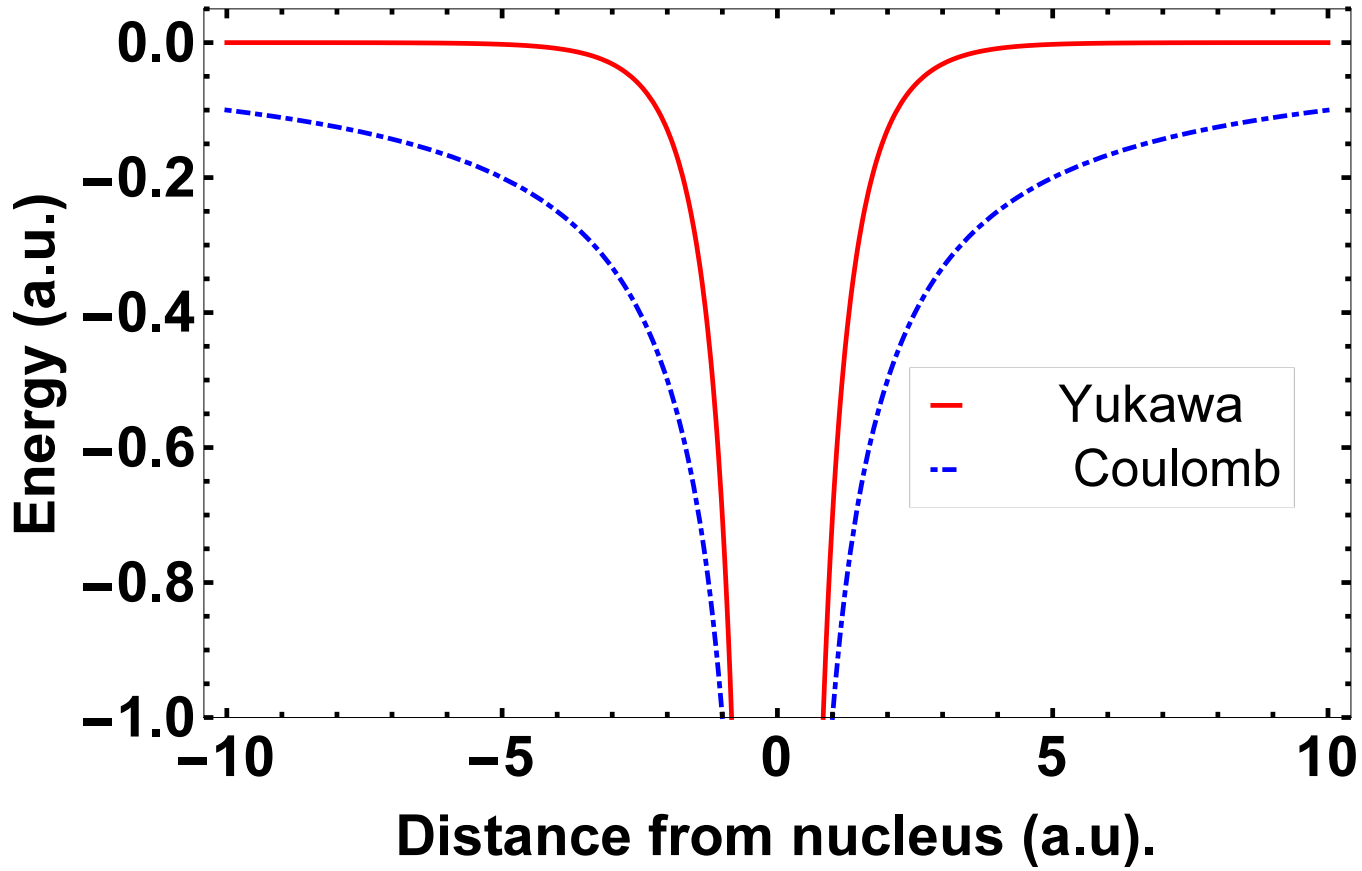


**Extended Data Fig. 3 | The Yukawa potential.** A short-range Yukawa potential was used to investigate the effects of the electric field of the resultant ion on the electron. The Yukawa potential (red line) is of the functional form $U_Y = -(Z/r) \times e^{-r/a}$, with parameters $Z = 1.90831$ and $a = 1$; $r$ is distance from the nucleus. It goes to zero quickly in comparison to its Coulomb counterpart (blue line). The parameters were chosen to retain the ground-state energy of H.

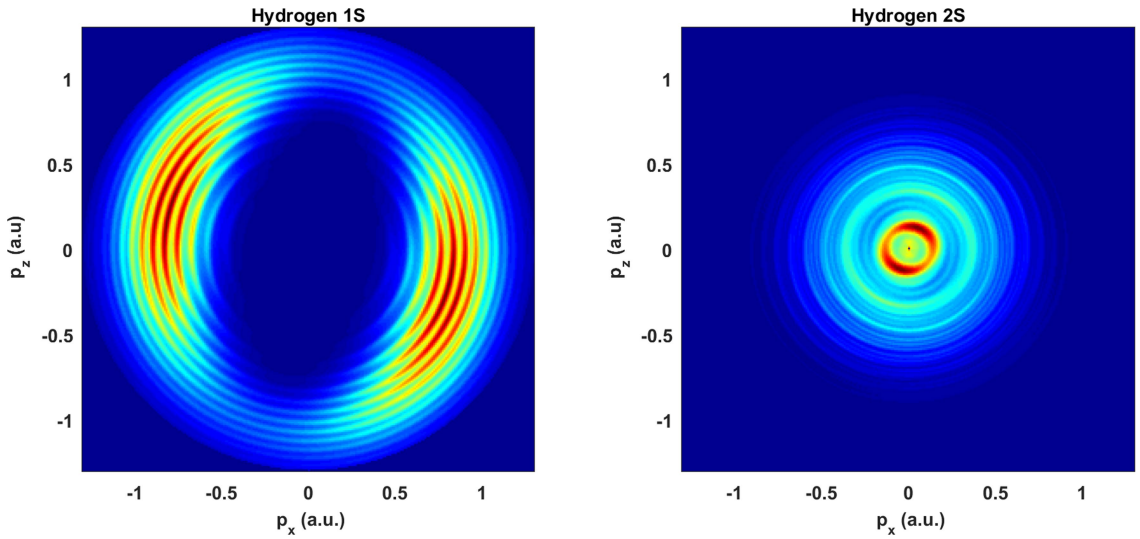


**Extended Data Fig. 4 | Simulated momentum distributions for 1*s* and 2*s* states of H.** Simulations performed for a peak intensity of $1.9 \times 10^{14}$ W cm$^{-2}$ are shown for initial states 1*s* (left) and 2*s* (right). It is clear that the metastable H 2*s* is characterized by less energetic electrons with nearly uniform angular distribution. The colour represents the relative probability of an electron having a particular momentum—from zero (dark blue) to the highest (red).